



American Society of  
Mechanical Engineers

**ASME Accepted Manuscript Repository**

**Institutional Repository Cover Sheet**

Cranfield Collection of E-Research - CERES

---

ASME Paper Title: Estimation of resultant airframe forces for a variable pitch fan operating in reverse thrust mode

---

Authors: David John Rajendran, Richard Tunstall, Vassilios Pachidis

---

ASME Conf Title: ASME Turbo Expo 2022: Turbomachinery Technical Conference and Exposition

---

Volume/Issue: Volume 1

Date of Publication (VOR\* Online) 28 October 2022

ASME Digital Collection

URL: <https://asmedigitalcollection.asme.org/GT/proceedings/GT2022/85970/V001T01A024/1148579>

---

DOI: <https://doi.org/10.1115/GT2022-82446>

---

\*VOR (version of record)

---

## ESTIMATION OF RESULTANT AIRFRAME FORCES FOR A VARIABLE PITCH FAN OPERATING IN REVERSE THRUST MODE

**David John Rajendran\***

Rolls-Royce UTC, Centre for Propulsion Engineering,  
Cranfield University,  
Cranfield, Bedfordshire, MK43 0AL, UK

e-mail: [d.rajendran@cranfield.ac.uk](mailto:d.rajendran@cranfield.ac.uk)

**Richard Tunstall**

Rolls-Royce plc,  
Bristol, BS34 7QE

e-mail: richard.tunstall@rolls-royce.com

**Vassilios Pachidis**

Rolls-Royce UTC, Centre for Propulsion Engineering,  
Cranfield University,  
Cranfield, Bedfordshire, MK43 0AL, UK

e-mail: v.pachidis@cranfield.ac.uk

### ABSTRACT

*The resultant forces with a reverse thrust Variable Pitch Fan (VPF) during the aircraft landing run are computed from the installed reverse thrust flow field obtained from an airframe-engine-VPF research model. The research model features a reverse flow capable VPF design in a future, geared, high-bypass ratio 40000 lbf engine as installed onto a twin-engine airframe in landing configuration, complete with a rolling ground plane to mimic the runway. The reverse thrust flow field during the aircraft landing run is obtained from 3D RANS/URANS solutions of the model. The evolution of the installed dynamic reverse thrust flow field is characterized by the interaction of the VPF induced reverse flow with the free stream. Several flow features like reverse flow wash-down by the freestream, external swirling helical flow development, pylon flow obstruction, 180° flow turn into the engine, subsequent separated flows, wake interactions and multi-pass recirculating flows are observed.*

*The resultant airframe forces due to the reverse thrust flow field is estimated by adaptations of momentum based far-field and near-field methods. In the active thrust reverser engagement regime of 140 to 40 knots, the VPF generates a sufficient axial airframe decelerating force in the range of 45% to 8% of maximum take-off thrust. A drag decomposition study and a notional 'blocked-fan'*

*analysis are described to understand the stack-up of the axial decelerating force. Additionally, the resultant force has a landing speed dependent lateral force component because of the pylon obstruction induced flow non-uniformity. A beneficial downforce component due to upward deflection of streamlines is also observed. The quantification of the resultant forces from the baseline installed airframe-engine-VPF reverse thrust flow field is a necessary step to explore the feasibility of the VPF reverse thrust system for future efficient turbofan architectures, understand force generation mechanisms and to identify areas for subsequent design improvement.*

Keywords: variable pitch fan, reverse thrust, feasibility study, installed flow field, far field and near field methods

## **INTRODUCTION**

A VPF, in which the stagger angle of the fan aerofoils can be varied, is a design proposition to effectively harness the benefits of high propulsive efficiencies in future efficient and environment friendly high bypass ratio civil turbofan engines. Aircraft and engine performance studies have demonstrated that the VPF is an attractive solution to manage and optimize the low-pressure ratio fan operation mandated by thermodynamic constraints in high bypass ratio engines. These studies have indicated that the use of VPF can improve the aircraft mission fuel burn by up to 7% [1-3]. Further, if the VPF is used to generate reverse thrust in the engine, the conventional nacelle-based cascade thrust reverser system, which would occupy a significant proportion of the aircraft weight budget due to the large nacelle diameters in high bypass ratio engines, can be eliminated. The elimination of the nacelle-based thrust reverser would open the design space for development of low installation drag ‘slim-line’ nacelles without any thickness constraints required to accommodate the reverser cascades. The cascade of benefits in using a reverse thrust capable VPF in reducing weight, installation drag and optimizing nominal engine operation in future ultra-high bypass ratio engines could reduce the aircraft mission fuel burn by up to 15% [1-4]. Therefore, a reverse thrust capable VPF can be a key technology enabler and differentiator in the development of low fuel burn, environment friendly aircraft, and aid in the march of the civil aviation sector towards NetZero targets [5].

The VPF can be used to change the direction of airflow through the fan, and thus generate reverse thrust, by rotating the aerofoils by around 90° about the stacking axis in either a ‘through-feather’ or ‘through-flat’ direction. Such rotation shifts the aerofoil cascade capture throat area toward the nominal fan outlet and induces reverse flow through the fan. Typically, ‘through-feather’ rotation (aerofoils transition to reverse flow mode position through a feather pitch setting as in propeller blades) is preferred to the ‘through-flat’ rotation (aerofoils transition through a blocked or flat pitch setting) to eliminate aerofoil tangling related solidity restrictions on optimal fan design. A schematic demonstrating the VPF aerofoil rotation to the reverse flow operation mode is shown in Appendix.

The use of VPF to reverse airflow in turbofan engines was studied by NASA in the Quiet Clean Short-haul Experimental Engine (QCSEE) and the Advanced Ducted Propulsor (ADP) programs. Both these programs focused on the development of reverse flow capable VPF turbomachinery designs which were explored in experimental rig settings that featured the VPF operating in uninstalled,

isolated, stand-alone models with engine-like flow paths. A low-pressure ratio, low noise VPF design that can be adapted for use in high bypass ratio engines was developed in the ADP program. The ADP VPF behavior at different forward and reverse flow settings was characterized in experimental and computational studies using a 22-inch isolated rig at static and limited forward flow conditions [6-8]. Beside these NASA programs, two legacy demonstrator engines with reverse flow VPF were also built: M.45SD-02 by Rolls-Royce, Dowty Rotol and Snecma, and NK-93 by Kuznetsov. The M.45SD-02 was tested in reverse flow in an isolated, static test bed to generate data on the fan performance and mechanical integrity [9]. A static test of the NK-93 engine is reported to have generated reverse flow with the VPF, although no details are available [10].

The key observation from the previous experimental and computational studies is that the VPF reverse flow behavior has been explored only in uninstalled, isolated, static, or limited dynamic conditions, often with several rig-level design modifications and simplifications. While these explorations have resulted in the capability to develop reverse flow VPF turbomachinery designs and validated the concept of establishing reverse flow in an isolated static engine, no studies have thence been done to understand the VPF reverse thrust behavior, as installed on to an airframe during the aircraft landing run. Therefore, to address this research gap, the authors developed an integrated airframe-engine-VPF model to computationally obtain the realistic installed dynamic VPF reverse thrust behavior during the aircraft landing run [11]. Several aspects of the VPF reverse thrust behavior like the installed dynamic fan flow field, distortion transferred on to the core engine inlet during reverse thrust operation and the use of an inflatable rubber lip to improve the reverse flow were discussed by the authors in separate publications [12-14].

Moreover, the few isolated, stand-alone engine tests conducted previously by NASA and the engine manufacturers have limited information on only the static, uninstalled VPF reverse thrust levels. However, if a VPF is to replace the cascade thrust reverser in a future aircraft, an estimation of the resultant decelerating forces on the airframe during the aircraft landing run is required to ascertain the feasibility of engineering the VPF reverse thrust system. Therefore, in this work the installed dynamic flow field obtained from the 3D RANS/URANS solutions of the integrated airframe-engine-VPF model with the VPF operating in reverse thrust mode during the aircraft landing run is used to estimate the resultant airframe forces by adaptations of momentum based far-field and near-field methods. The resultant airframe forces are discussed in the paper by resolving their components to quantify the axial decelerating force and shed light on the hitherto undescribed lateral and pitch force components. Since the resultant axial decelerating force represents the total aerodynamic braking force on the aircraft, a drag decomposition analysis is carried out to separate the contribution of the airframe drag

without reverse flow and estimate the VPF reverse thrust contribution. Additionally, a notional ‘blocked-fan’ analysis is also discussed to understand the contribution of different physical mechanisms like the flow reversal and blockage to the VPF reverse thrust.

## **INTEGRATED AIRFRAME-ENGINE-VPF MODEL**

### **Model Description**

A representative integrated airframe-engine-VPF model with a VPF operating in reverse thrust mode in a typical future high-bypass ratio geared turbofan engine as installed on to a 300-seater twin-engine airframe is used to generate the dynamic installed reverse thrust flow field and estimate the resultant airframe forces during the aircraft landing run. The engine design is optimized with a design bypass ratio of 14 and sized to produce 40000 lbf at maximum take-off conditions to meet the airframe requirements. The engine design is typical of future high-bypass ratio architectures in which the VPF is used to optimize nominal operation during different phases of the aircraft mission profile. The engine model features a full 360° annulus representation of the bypass nozzle flowpath that includes the pylon bifurcation strut, Outlet Guide Vane (OGV) blade row, core engine splitter, VPF aerofoil row and fan spinner, all of which are designed following conventional modern turbofan practice using in-house design tools. Parts of the core engine like the core entry duct, exhaust duct, core nozzle and aft-body plug are also included to appropriately interface with the external airframe and bypass flowpath model. A representation of the airframe-engine-VPF model with a portion of the discretized domain is shown in Figure 1.

The VPF and OGV turbomachinery designs are developed from the validated NASA ADP rig design. The hub-to-tip ratio of the VPF is modified to 0.3 from the ADP rig value of 0.42, with optimized spanwise aerofoil stagger angle and thickness distributions to maintain the same flow coefficient-stage loading distribution of the baseline design, while being representative of high efficiency fan designs in future high bypass ratio engines. The VPF in nominal operation is designed to meet the optimized engine performance cycle requirements of 1.27 pressure ratio, 1.08 temperature ratio with a tip speed of 245 m/s at the design point. No restrictions on the blade row solidity are considered in the VPF design since it is conceived to transition to reverse flow operation mode ‘through-feather’ transition as in the ADP rig. The reverse flow behavior of the VPF blade row in isolation is computationally characterized for different combinations of reverse mode stagger angle settings and rotational speeds. Two stagger angle settings,  $\zeta_1^\circ$  and  $\zeta_2^\circ = \zeta_1^\circ - 6^\circ$  (both values within  $\pm 10^\circ$  from the reference  $90^\circ$  rotated reverse flow setting) are chosen for detailed exploration in the integrated model based on their wide mass flow (up to 0.55x of design mass flow) and pressure ratio (1.1 to 1.2) trends from the isolated VPF reverse flow characteristics. Each of the stagger angle settings are explored at bounds of rotational speed,  $N_1$  and  $N_2 = 0.8N_1$ , which are within  $\pm 15\%$  of fan design speed to understand the effect of fan power setting.

The VPF at the two different stagger angle settings along with the complete engine internal flowpath are wrapped in an axisymmetric nacelle and installed onto the airframe through a bespoke pylon design. The nacelle and pylon designs are developed through a detailed

installation aerodynamics study to be representative of modern airframe designs. The 300-seater, twin engine airframe with the wings, flaps, slats, and spoilers deployed in landing configuration is developed from a baseline DLR F11 airframe that is used for studying high-lift flows. Each component of the integrated model is individually validated: the VPF using benchmark NASA ADP experiments, the airframe using forward flow coefficient of pressure distribution from wind-tunnel data used in code validation studies and the engine flow path by comparison with typical modern turbofan architectures. The computational domain is defined by a half of the airframe-engine-VPF model placed in a cuboidal far field domain with all its faces, except the base and the symmetry plane, at least 20 engine diameters away from airframe extremities. The domain is bounded in its base by a translating plane to mimic the rolling runway during the aircraft landing run. A typical engine ground clearance of 0.6 m is considered to place the airframe-engine-VPF model with reference to the ground plane. The integrated airframe-engine-VPF model is built in this manner to quantify the amount of the decelerating force that a reverse thrust VPF would generate during the landing run of a typical modern airframe installed with a future high bypass ratio turbofan engine and no additional reverse thrust specific design features. Further details of the VPF turbomachinery design, engine components and airframe design, along with a detailed exploration into the benefits of using an integrated model for VPF reverse thrust studies are discussed in a separate model development paper by the authors [11].

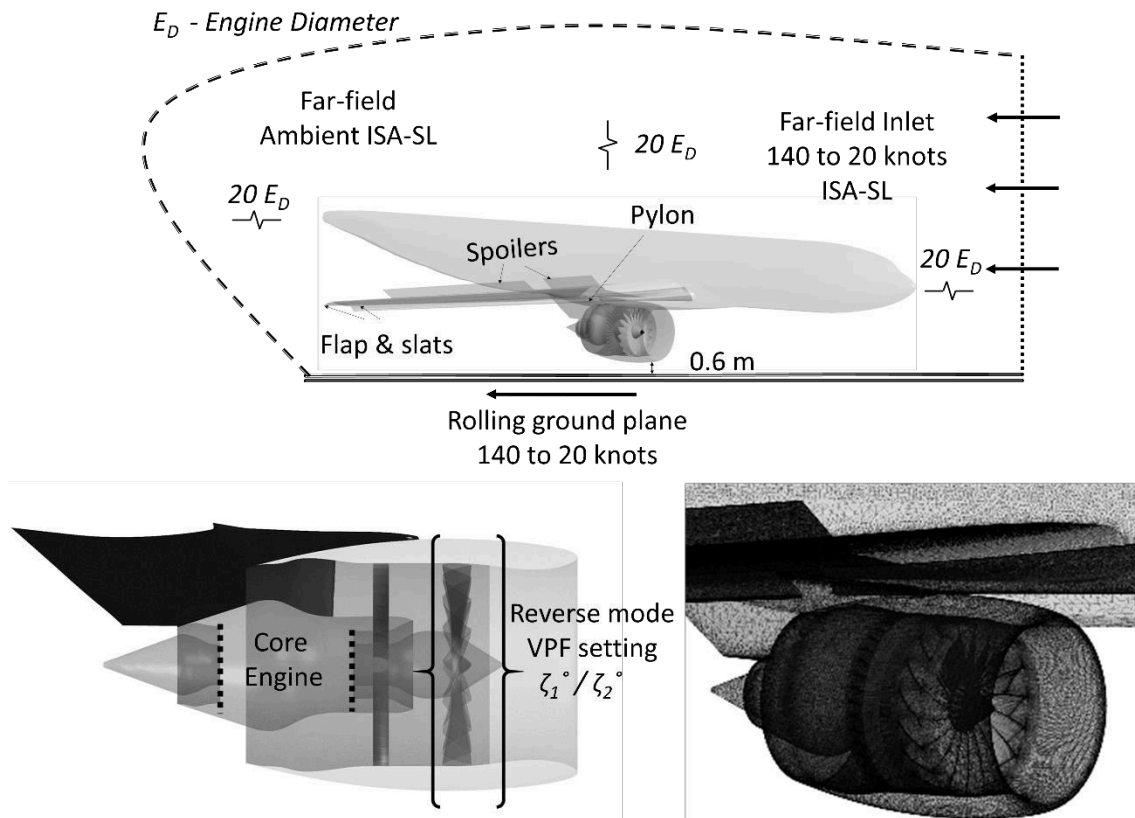


**FIGURE 1: SCHEMATIC OF AIRFRAME-ENGINE-VPF RESEARCH MODEL [12]**

## Computational Solution Methods

The computational domain is discretized using a hybrid approach with both unstructured and multi-block structured topologies. The grid elements are ensured to have determinant quality, skew, aspect ratios and near-wall expansion ratios within typical best practice guidelines. Extensive Grid Convergence Index (GCI) estimation studies are carried out by considering all the global and local parameters of interest to finalize a total grid size of ~73 million elements. A gross GCI parameter computed statistically from zonal flow and global parameters using the Richardson extrapolation method is not more than 0.006.

The computational problem for the VPF geometry at a stagger angle setting is numerically well-posed by the specification of flux preserving general fluid-fluid interfaces at each of the stationary component boundaries, frame-change interfaces at the intake-VPF and the VPF-splitter boundaries, the VPF rotational speed, flow velocity at the far field inlet, ground plane translational velocity, far field ambient conditions and core engine boundary conditions. Detailed frame-change interface independency for the global parameters of interest is verified and a frozen rotor interface is selected to preserve the convection of the complex 3D non-axisymmetric flow field across the stationary-rotating domain interface. The flow velocities at the far field inlet and the ground translational velocity are the same as the aircraft landing speed. The core engine boundary conditions are specified in terms of axial velocity and total temperature values obtained from the engine thermodynamic performance model at the landing throttle setting [12, 15]. All the wall boundaries are specified as no-slip adiabatic walls.

The flow solutions are obtained from a typical touchdown velocity of 140 knots to typical thrust reverser shutdown velocity of 40 knots for each VPF stagger angle ( $\zeta_1^\circ$  or  $\zeta_2^\circ$ )-rotational speed (N1 or N2) combination. Exploratory 3D RANS solutions of the flow field obtained using ANSYS-CFX, a coupled finite volume implicit solver, indicated the presence of residual unsteadiness and time-varying flow field features. Therefore, time-averaged 3D URANS solutions are generated to estimate the decelerating forces at a particular VPF operating point for all landing speeds. These results are compared with subsequently refined 3D RANS solutions obtained from domain dependent, convection velocity-based physical timescales and a convergence strategy that takes into account the resolution of parameter changes due to unsteady effects [12]. It is noted that the computed decelerating force results from both the approaches are within 2%. Subsequent detailed parametric exploration of decelerating forces is done using 3D RANS solutions. The conservation and turbulence closure equations are numerically solved by higher order spatial resolution schemes with non-linear blending interpolation functions that ensure higher order accuracy while eliminating dissipative errors. Turbulence closure is modelled by using the two-equation  $k-\omega$  shear stress transport model. Near-wall flow physics is explicitly resolved by grid refinement. The transient terms are discretized using a robust, implicit, time-conservative second order backward Euler scheme. The unsteady timestep, which is in the order of 10-6 s, is selected based on the driving VPF turbomachinery domain physical timescales with each VPF rotation discretized in

100 steps. The consistency of the chosen timestep with the stability and convergence requirements of the solver is verified by ensuring that the Courant number is less than 1 within the engine internal flow path and the near vicinity of the airframe-engine. Timestep independence of the unsteady solution is ensured by comparing the results obtained from 3 timestep choices viz. half, double and a non-harmonic fraction of the chosen physical timestep. The use of a moving mesh, sliding interface, transient blade row model as against the unsteady frozen rotor interface is found to have a difference of less than 1% in the bulk flow parameters of interest. Therefore, the frozen rotor unsteady frame change model is considered for the averaged flow field generation because it can accurately capture the relevant flow phenomena with an order of magnitude reduction in time, storage, and processor requirements.

The computations are carried out in a 60 Teraflops, 1888 core high performance computing facility 'DELTA' using a platform message passing interface parallelization scheme. Owing to the large size of the computational domain, an optimized recursive coordinate bisection algorithm is used for partitioning along with overrides of up to 500% for memory allocation. The spatial flow field convergence is monitored by defining change threshold values of less than 0.5% in parameters of interest between iteration block standard deviation and mean values. Temporal convergence is monitored by statistical processing of flow parameter evolutionary traces and ensuring less than 0.5% change threshold in the calculated wave parameters over specified timestep blocks. The flow results are averaged over a periodic timestep block after spatial and temporal convergence criteria are met. The computational time in the 3D URANS runs for one timestep is 24 minutes, and typically 2500 to 3000 timesteps are required for flow development and meeting the convergence criteria, requiring nearly 650 to 750 hours of computational time for each aircraft landing speed. Details of the model development, computational domain discretization and computational solution methods are discussed in further detail in other publications by the authors [11-14].

## **REVERSE THRUST FLOW FIELD**

The VPF reverse thrust flow field at a representative landing speed is shown in Figure 2 using projected streamlines on an engine mid-surface plane that extends into the external regions around the engine to highlight the general flow field features. In the reverse thrust mode, flow swirls out of the fan towards the nacelle inlet along the outer annular regions. The freestream flow ingresses into the nacelle intake inner annular regions and is entrained by the reverse flow out of the fan. As the reverse flow reaches the nacelle lip, it is washed down externally over the nacelle outer cover by the freestream towards the engine exit regions. As the washed down reverse stream reaches the bypass nozzle exit, it comes under the influence of the fan suction and turns 180° into the engine resulting in a large separation at the bypass nozzle lip. The flow stream that escapes the VPF suction at the engine exit is deflected radially upwards due to the nacelle contour near the ground plane and the pylon interference which obstructs the balancing radially downward flow from the nacelle upper surface. As the reverse flow develops within the engine towards the VPF passages, a portion of the flow turns 180° at the



splitter edge to feed the core engine. The remaining flow which enters the VPF meets the freestream in a shear layer and is centrifuged radially outwards. A portion of the centrifuged flow is turned back towards the bypass nozzle exit as it reaches the fan outer annulus, and passes through the OGV blade row, where it loses momentum and rejoins the reverse flow towards the VPF (marked as turned back reverse stream in Figure 2 – ‘Internal’). Another portion along with the entrained free stream flow sets up the reverse flow out of the VPF.

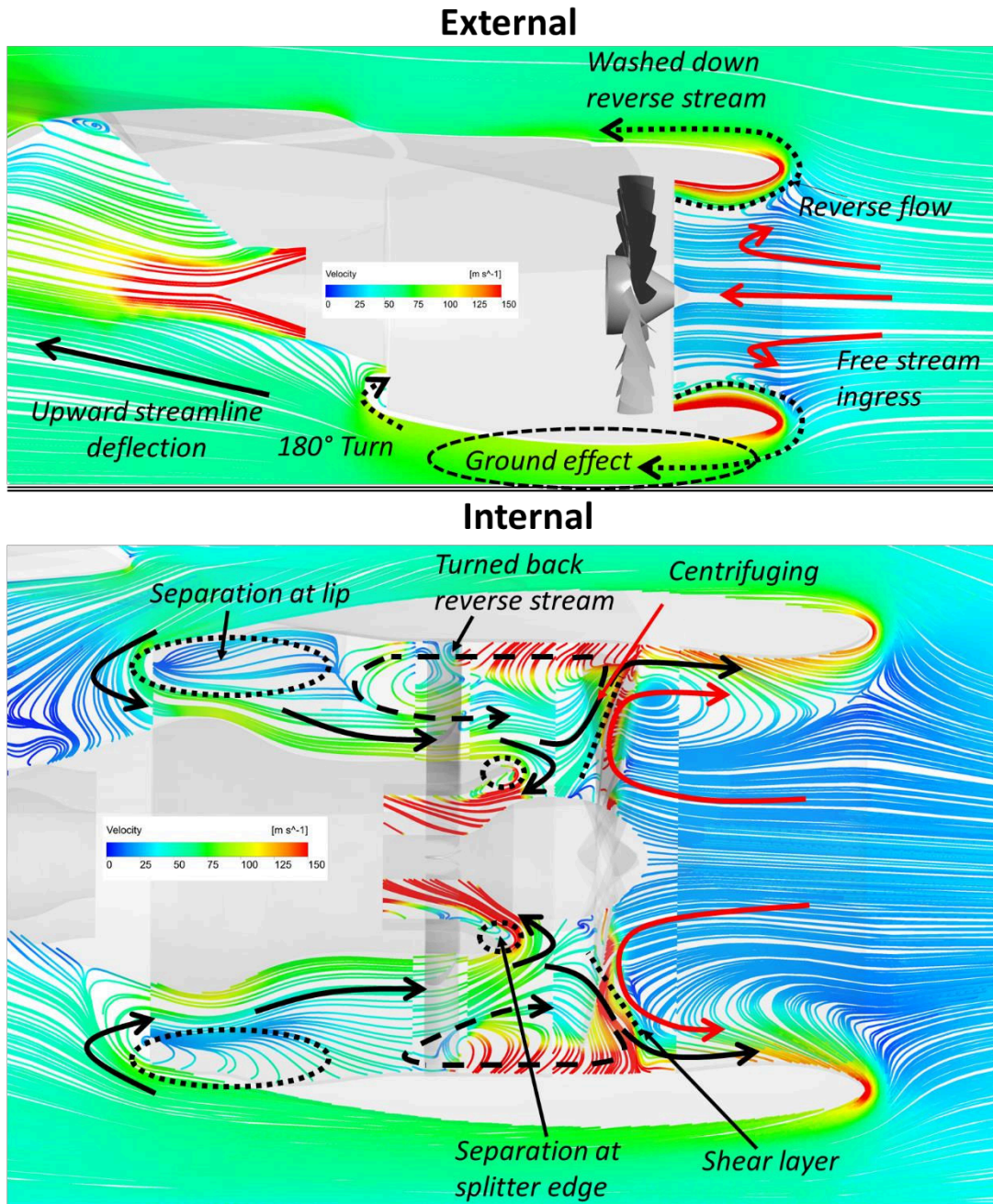


**FIGURE 2:** GENERAL FEATURES OF VPF REVERSE THRUST FLOW FIELD [13]

The extent of the afore mentioned reverse thrust flow field features change with the aircraft landing speed due to the reduction in the free stream momentum as the aircraft decelerates on the runway. These are shown in Figure 3 using the reverse flow streamlines from the VPF inlet at different landing speeds from 140 to 20 knots.

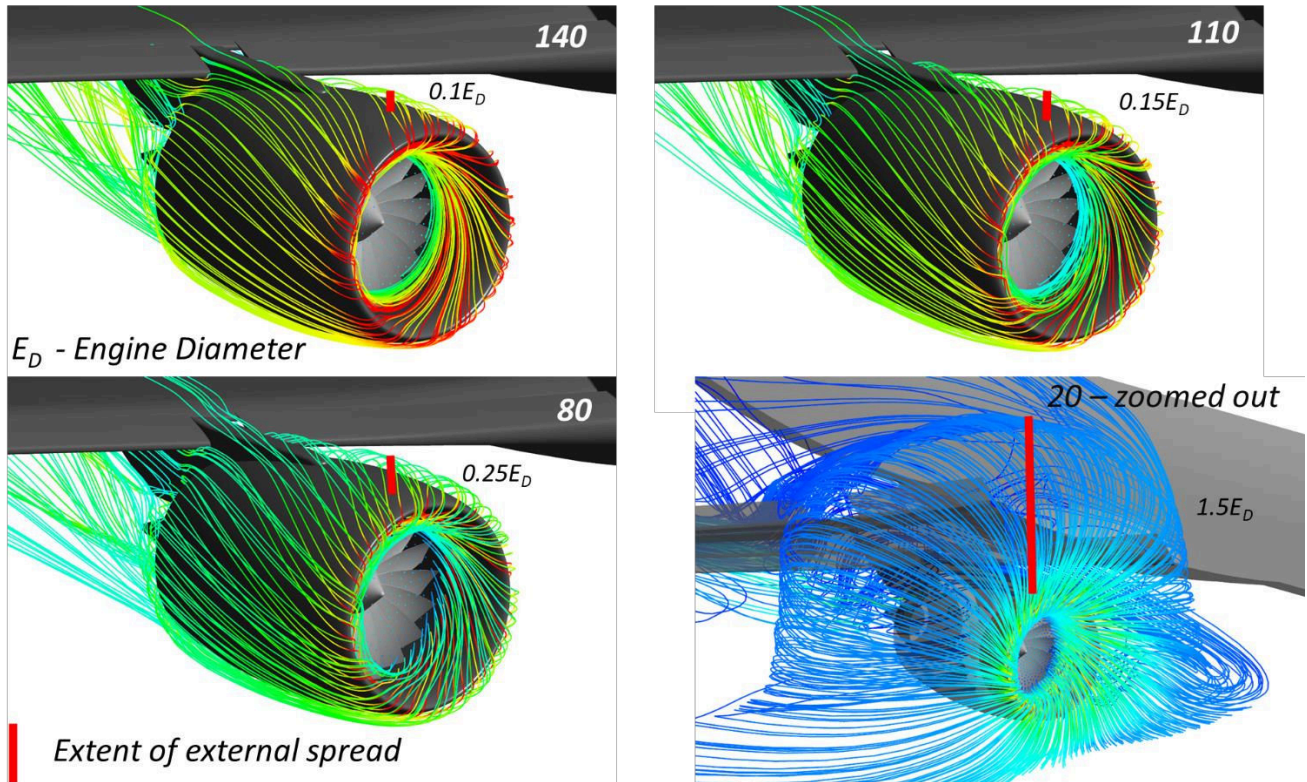


**FIGURE 3:** EXTERNAL REVERSE THRUST FLOW FIELD AT DIFFERENT LANDING SPEEDS

As the aircraft landing speed decreases, the reverse flow streamlines that are washed down by the freestream at the nacelle inlet progressively extend further around the engine because of the reduction in the freestream momentum, as shown by the red markers in Figure 3. Down to a landing speed of 40 knots, the washed down reverse stream sticks around the nacelle outer cover to reach the engine exit at a swirl angle. The swirl angle consequently results in flow accumulation in the pylon outboard side. The reverse flow shrouding extent around the engine varies from  $0.1E_D$  to  $0.4E_D$  in the 140 to 40 knots range. However, as the aircraft decelerates below 40 knots, the momentum balance skews in favor of the reverse stream in such a way that it lifts from the nacelle lip and spreads around the engine in a flow pattern that looks like a ‘peacock-dance’. In the engine regions near the ground, the vertical spread of the streamlines is blocked by the ground which causes it to spread out laterally. The extent of reverse stream lift-up above the engine before it is turned around by the bulk freestream flow varies from  $1.0E_D$  to  $1.75E_D$  in the 30 to 10 knots range; the lateral spread in the engine lower region is up to  $1.0E_D$  in either direction. In the limiting case, where there is no free stream flow, there is no turn-around of the reverse flow streamlines and the reverse flow exists as a jet piercing ahead of the engine front face into the far field. It is emphasized here that in typical aircraft

landing routine, the thrust reverser is often disengaged at about 40 knots to prevent foreign object damage and thus the ‘peacock-dance’ flow field may not occur in routine landing usage.

Moreover, as the freestream momentum reduces, a larger amount of slower moving flow in the engine exit regions comes under the influence of fan suction, which results in an increase in the reverse stream mass flow into the engine from 25% to 55% of reference nominal mass flow in the 140 to 20 knots range. This increase causes a minor redistribution in the internal flow field features and an increase in the reverse flow out of the fan, which further contributes to the dominance of the reverse stream momentum at lower landing speeds. Further details of the non-uniform internal and fan flow field at different landing speeds are described in the work on installed fan flow field by the authors [12].

## FORCE ESTIMATION METHODS

### Near Field and Far Field Methods

Momentum equation based near field and far field methods that are typically used in aircraft thrust-drag bookkeeping studies are used to estimate the resultant airframe forces due to the reverse thrust flow field during the landing run. Momentum conservation is applied over a control volume that encapsulates all the fluid wetted body surfaces and extends into the far field to define flux surfaces through which the fluid traverses. The near field force term is obtained from the integral of the pressure and shear distributions on the airframe and engine body surfaces:

$$F_{Near} = \iint_{body\ surfaces} [-pn + \tau \cdot n] dS \quad (1)$$

Where  $F_{Near}$  is the resultant near field force vector,  $\tau$  is the shear stress tensor obtained from wall shear flow solution data,  $p$  is the pressure term and  $n$  is the normal vector of the elemental surface area. The far field integral at a flux surface is computed from the convective flux integral and the pressure-shear stress distribution on the flux surface:

$$\varphi_{flux\ surface} = \iint_{flux\ surface} -(\rho V \cdot dS)V + \iint_{flux\ surface} (-pn + \tau \cdot n)dS \quad (2)$$

Where  $\varphi_{flux\ surface}$  is the far field integral at a control volume flux surface, on the RHS: first term is the convective flux integral and second term is the correction for pressure-shear distribution on the flux surface,  $V$  is the velocity vector and  $\rho$  is the density term. The boundaries of the core engine inlet and outlet are also flux surfaces in addition to the control surfaces in the far field domain. The far field force term is then evaluated from a summation of all the control volume flux surface far field integral terms:

$$F_{Far} = \sum \varphi_{flux\ surface} \quad (3)$$

The equality of the near field and far field force terms, as dictated by momentum conservation, is used to verify numerical integral computation, assess the flow parameters linked with the force terms through allied conservative physical flow mechanisms and cross validate the resultant force estimates. The independence of the far field force term to the location and size of the control volume is verified by checking the momentum conservation over several progressively increasing control volume sizes. A fixed control volume definition with the control flux surfaces  $3E_D$  upstream,  $5E_D$  downstream,  $2E_D$  to the left and right,  $3E_D$  to the top from the engine inlet center point reference plane and the bottom surface 0.05 cm above the ground plane is chosen to ensure similar grid element level resolutions and optimal computational cost during the numerical integration for flow fields at different landing speeds. The fixed control volume with explicit resolution of control surface forces is preferred over the use of bounding stream tube for the control surfaces because the change in the bounding stream tube location with landing speed results in different levels of resolution and consequent added uncertainties during the numerical integral evaluation. The total uncertainties in the force estimation due to numerical integral evaluations (particularly from high curvature regions in the near field terms and control surface size in the far field terms) lead to a conservation imbalance of not more than 2% in all computations. The resultant airframe force vector consists of the axial decelerating force ( $F_z$ ), lateral force ( $F_y$ ), and pitch force components ( $F_x$ ).

### **Drag Decomposition Analysis**

The resultant airframe forces with the thrust reverser engaged represents the total aerodynamic braking force felt on the aircraft during the landing run. Additionally, it is desirable to separate out the contribution of the VPF reverse thrust from the axial decelerating force component to define a reverse thrust term,  $F_{RT}$ . In this study, this reverse thrust term is defined by subtracting the drag force felt on the baseline airframe without the thrust reverser engaged,  $D_{no\_RT}$ , from the axial decelerating force generated with the thrust reverser,  $F_z$ . The drag force on the baseline airframe is obtained for the complete landing run from a separate set of 3D RANS analyses of the integrated model without the VPF in reverse mode. In the drag estimation runs, the mass flow at the VPF inlet is distributed between the bypass nozzle and the core engine nozzle based on the bypass ratio at the engine landing throttle setting performance data to mimic the normal landing operation without reverse thrust. All the components of the airframe in the landing configuration including the spoilers, flaps, slats along with the rolling ground plane that represents the runway movement as in the integrated airframe-engine-VPF model are included in the drag estimation runs to separate out only the VPF contribution to reverse thrust.

The baseline airframe drag without reverse thrust is computed using the momentum-based methods applied on the same control volume as in the reverse thrust runs. The airframe coefficient of drag without the thrust reverser is computed to be 0.015, which translates to 11% to 1% of the engine maximum take-off thrust in the 140 to 40 knots landing speed range. The computed drag coefficient without reverse thrust is comparable to the experimental drag coefficient of the seed DLR F11 airframe that features similar airframe control

surfaces in landing configuration, and to which are added the additional effects of spoilers at 50° deployment angle and nacelle-pylon-wing installation drag [16, 17]. The computed value is also in the same ballpark as the values for similar family of modern twin engine airframes (0.014 to 0.018) [18, 19]. It is emphasized that the resultant decelerating force with the reverse thrust engaged is the primary parameter of interest for assessing the aircraft landing performance and this decomposition of the decelerating force into a no reverse thrust drag component and the VPF reverse thrust contribution is done to appreciate the extent of increase in the decelerating force over the case in which the thrust reversers are not engaged.

## RESULTANT AIRFRAME DECELERATING FORCES

The primary purpose of the reverse thrust VPF is to generate an axial decelerating force,  $F_z$ , on the airframe during the landing run. The lateral force,  $F_y$ , and the pitch force,  $F_x$ , are secondary features that appear because of the reverse thrust flow field. Therefore, in this section, the decelerating force  $F_z$  during the complete landing run is discussed first for different VPF operating conditions in terms of rotational speeds and stagger angle settings. The decelerating force is separated into the VPF reverse thrust contribution, and the baseline airframe drag using the drag decomposition analysis. Additionally, the results from a notional ‘blocked fan’ analysis are also presented to understand the key mechanisms that make up the VPF reverse thrust contribution to the axial decelerating force. Thereafter, the lateral and pitch force components are discussed along with the flow mechanisms that give rise to these secondary components.

### Axial Decelerating Force

The axial decelerating force on the airframe,  $F_z$ , the VPF reverse thrust contribution,  $F_{RT}$ , and the airframe drag without the reverse thrust engaged,  $D_{no\_RT}$ , when the VPF is at  $\zeta_l^\circ$  stagger angle setting and a rotational speed of  $N_l$  is shown in Figure 4. The force values are nondimensionalized with the maximum rated engine thrust at take-off condition,  $T_{MTO}$ . The decelerating force profile is shown for the aircraft landing run during the typical thrust reverser engagement regime of 140 to 40 knots. The axial decelerating force varies from 45% of  $T_{MTO}$  at the aircraft touchdown to 8% of  $T_{MTO}$  at the thrust reverser shutdown with a typical decreasing trend that is proportional to the dynamic head ( $\rho V^2$ ). The VPF thrust reverser contribution to the axial decelerating force varies from 34% to 7% of  $T_{MTO}$ , which is over and above the baseline airframe drag contribution of 11% to 1% of  $T_{MTO}$  in the same landing speed range. The VPF thrust reverser contribution values are in the similar range as the typical reverse thrust parameters used for landing performance calculations in aircraft mission simulation suites like NASA FLOPS and PIANO [20, 21]. The mission profile simulation suites typically use a constant 30% of design thrust as the reverse thrust during the entire aircraft landing run without accounting for the dynamic pressure driven reduction in the reverse thrust. Moreover, the reverse thrust values in the present study are normalized with the maximum take-off thrust, which is typically around 20% higher than the design thrust. Further, a typical target of 30% of design thrust is specified

as a target for novel thrust reverser concepts in technology demonstrator programs [22]. A free-body force diagram based integral landing distance calculation for the aircraft configuration with the computed VPF reverse thrust profile indicates that a similar reduction in aircraft ground run distances as in the cases with conventional thrust reversal systems in the aircraft mission analysis suites can be achieved with the reverse thrust VPF as well.

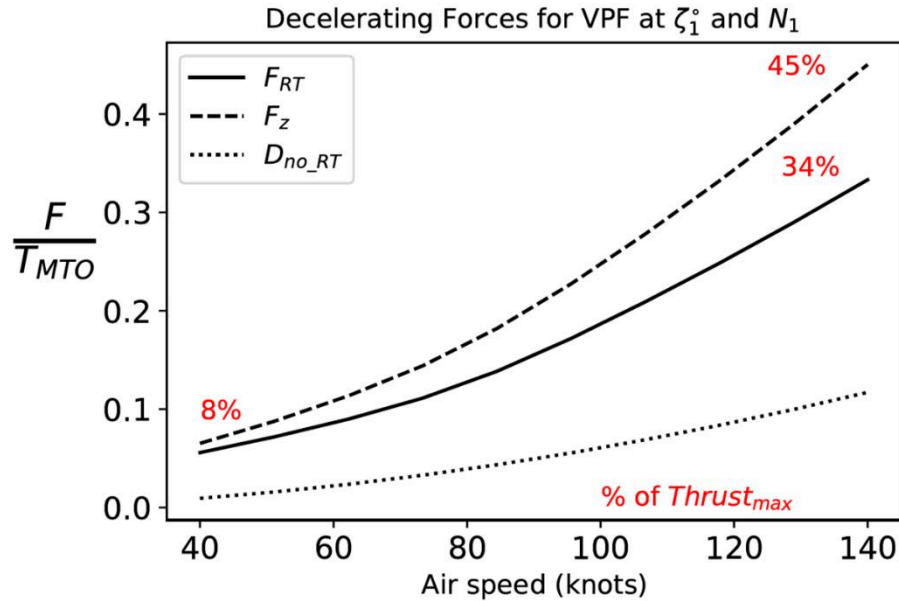


**FIGURE 4:** AXIAL DECELERATING FORCES FOR VPF AT  $\zeta_1^\circ$  STAGGER ANGLE AND  $N_1$  ROTATIONAL SPEED

The effect of fan rotational speed on the axial decelerating force and the VPF contribution to reverse thrust at a constant stagger angle setting of  $\zeta_1^\circ$  are shown in Figure 5. The rotational speeds shown in the figure,  $N_1$  and  $N_2=0.8N_1$ , represent the typical bounds of rotational speed based on engine operational settings during the landing run. The axial decelerating force and VPF reverse thrust contribution are marginally higher by 0.6% to 1.7% of  $T_{MTO}$  for the lower rotational  $N_2$ . This minor increase in the decelerating force is more pronounced in the lower landing speeds. There are two reasons that are responsible for this behavior: 1. Core Forward Thrust: The change in the core engine thermodynamic equilibrium with the reduction in VPF rotational speed results in a reduction in core forward thrust by 1.4% of  $T_{MTO}$ . The reduction in the core forward thrust appears as an increase in the reverse thrust and axial decelerating force at the lower rotational speed. 2. Change in Fan Reverse Thrust Flow Field: A reduction in the fan rotational speed results in a reduction of the reverse stream flow entering into the VPF nominal outlet plane. The flow entering the VPF nominal outlet, after a proportionally lower amount of flow enters the core engine, is distributed between the reverse flow exiting the VPF nominal inlet towards the engine external regions that contributes to reverse thrust and the flow turning back into engine towards the bypass nozzle as shown in the internal flow field of Figure 2. The breakdown of the flow between these streams is dictated by the freestream momentum which sets up an effective backpressure for the reverse flow exiting the VPF inlet. Consequently, at higher landing speeds lower amount of reverse

flow that contributes to the reverse thrust exit out of the VPF inlet due to the higher freestream momentum that pushes more flow into the engine at the VPF outlet. This reduction in reverse flow out of the engine inlet tempers the benefit accrued by the reduction in the core forward thrust at higher landing speeds. However, at lower speeds with the reduction in freestream velocity, the reduction in the flow out of the fan is not as pronounced and the full benefit of the lower core forward thrust is translated to the axial decelerating force.

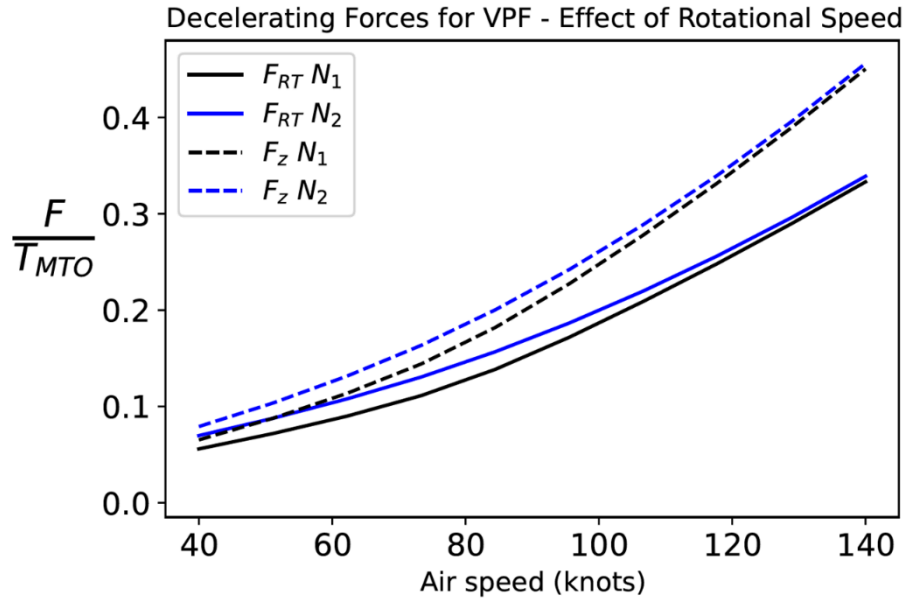


**FIGURE 5: EFFECT OF ROTATIONAL SPEED ON AXIAL DECELERATING FORCES AT  $\zeta_1^\circ$  STAGGER ANGLE**

The similar levels of axial decelerating force at lower fan rotational speeds means that the reverse thrust VPF can be operated at more benign, lower mechanical stress engine operating points to generate the necessary reverse thrust during the aircraft landing run. The trends of the axial decelerating force with the fan rotational speed also demonstrates the benefit of using the integrated airframe-engine-VPF model with proper resolution of the core engine thermodynamic operating point to study the reverse thrust behavior. A simple VPF only, uninstalled analysis, as was attempted in the literature before the present studies, would have presented a misleading picture of the reverse thrust trends by considering only the mass flow change with rotational speed change.

The change in fan stagger angle setting from  $\zeta_1^\circ$  to  $\zeta_2^\circ = \zeta_1^\circ - 6^\circ$  at either of the fan rotational speeds does not significantly affect the axial decelerating forces. These stagger angles are chosen for exploration in the integrated model due to their wide mass flow characteristics from the VPF reverse flow characterization study and indicate bounds of effective reverse flow settings that are within  $\pm 10^\circ$  from the reference  $90^\circ$  ‘through feather’ rotated reverse flow setting. The reason for the independence of the axial decelerating force is explained by the changes in the installed dynamic VPF fan flow field for the stagger angle settings, which are shown using the mean section blade-to-blade velocity contours for the two stagger angle settings in Figure 6.

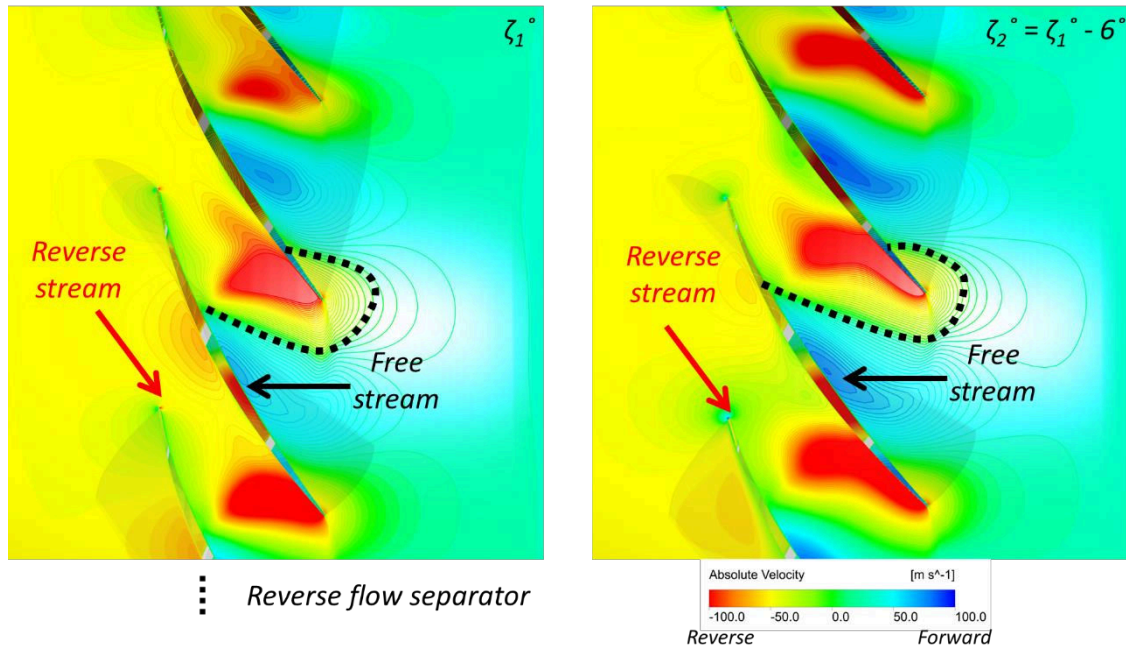


**FIGURE 6:** MEAN BLADE-TO-BLADE VELOCITY CONTOURS FOR  $\zeta_1^\circ$  AND  $\zeta_2^\circ$  STAGGER ANGLE SETTINGS

The  $\zeta_2^\circ$  stagger angle setting has more open fan aerofoil passages than the  $\zeta_1^\circ$  stagger angle setting. Therefore, a larger amount of reverse flow enters the VPF nominal outlet in the  $\zeta_2^\circ$  stagger angle setting. However, since the passages are also more open from the VPF nominal inlet, a larger amount of freestream flow penetrates further into the VPF passages and presents a larger blockage to the reverse stream from the VPF nominal outlet. Consequently, in the  $\zeta_2^\circ$  stagger angle setting a larger proportion of the reverse stream is turned back towards the bypass nozzle, resulting in similar amounts of flow exiting the VPF nominal inlet. Therefore, the more open  $\zeta_2^\circ$  stagger angle setting also indicates similar axial decelerating force levels because of the similar amount of net reverse flow exiting the VPF inlet that sets up equivalent external flow interactions as in the  $\zeta_1^\circ$  stagger angle setting.

The observed independence in the axial decelerating forces to the stagger angle setting indicates a possible freedom in the selection of VPF settings from considerations other than the reverse thrust performance like mechanical stressing or acoustic behavior. The importance of considering the dynamic flow field with the freestream modelled in estimating reverse thrust results is also demonstrated from the effect of decelerating force to changes in the stagger angle setting. Simple isolated engine, static VPF reverse flow explorations without the freestream effect modelled would indicate an increase in reverse thrust with the more open stagger angle settings, which would not be observed in actual dynamic operating conditions during the aircraft landing run.

#### Notional ‘Blocked Fan’ Analysis

The reversal of airflow within the engine and subsequent development of the reversed flow around the engine in the vicinity of the airframe is the reason for the increase in decelerating force on the airframe with the VPF in reverse thrust mode. In the previous section,



the axial decelerating force was decomposed into the VPF contribution to reverse thrust and the baseline airframe drag without thrust reverser engagement. Further, it is desirable to understand the VPF contribution to reverse thrust by deconstructing it into two driving physical flow mechanisms: 1. The reverse flow out of the engine preventing the forward flow to enter and flow through the fan. 2. The development of reverse flow within the engine and its subsequent development around the engine. Such a separation would deconstruct the VPF contribution to reverse thrust into two parts: 1. The part due to the blockage to the flow entering the engine in the nominal forward flow direction, termed the blockage effect. 2. The part due to the ingestion, ejection, and subsequent development of the reverse flow around the engine, termed the flow reversal effect.

In order to separate out the contribution of the blockage effect, a notional ‘blocked fan’ computational model is conceived. In the ‘blocked fan’ conceptual model, the fan inlet interface of the integrated airframe engine-VPF model is specified as a wall through which no flow can enter, the engine internal flow path components are removed since there is no need for internal flow resolution and the outlet faces in the bypass and core nozzle are also specified as walls because no flow is allowed to feed the nozzles. All the remaining features of the integrated airframe-engine-VPF model including the rolling runway are retained. The ‘blocked fan’ model is solved for the typical thrust reverser engagement regime of 140 to 40 knots during the aircraft landing run using a similar computational set up as the baseline model. The setup of the ‘blocked fan’ model and representative streamlines in a transverse plane that cuts through the engine into the external regions around the airframe at a landing speed of 110 knots is shown in Figure 7.

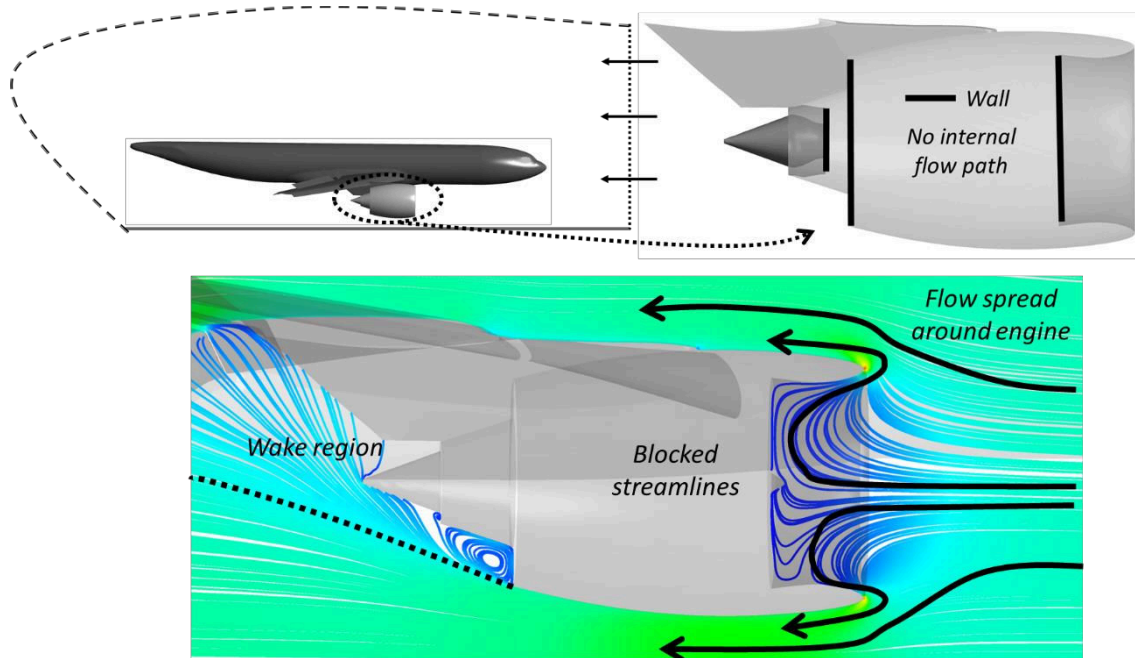


**FIGURE 7: NOTIONAL ‘BLOCKED FAN’ MODEL WITH STREAMLINES**

In the ‘blocked fan’ flow field, the freestream flow that enters the nacelle inlet is blocked by the wall specified at the fan interface. This obstruction is felt upstream of the engine and causes the freestream flow to spread around the engine. A large wake region develops behind the engine due to freestream blockage at the fan inlet, and the consequent prevention of flow development through the engine and the lack of exhaust flows from the bypass and the core nozzles. The resultant decelerating forces in the ‘blocked fan’ flow field during the thrust reverser engagement landing speed regime, as computed from the same control volume near field and far field formulations used in the reverse thrust estimation cases are shown in Figure 8. The axial decelerating force with the VPF in reverse thrust mode for the  $\zeta_l$  ° stagger angle,  $N_l$  rotational speed setting and the no reverse thrust airframe drag are included in Figure 8. The deconstruction of the VPF contribution to reverse thrust ( $F_{RT} = F_z - D_{no\_RT}$ ), into the blockage effect and the flow reversal effect is shown in Figure 9.

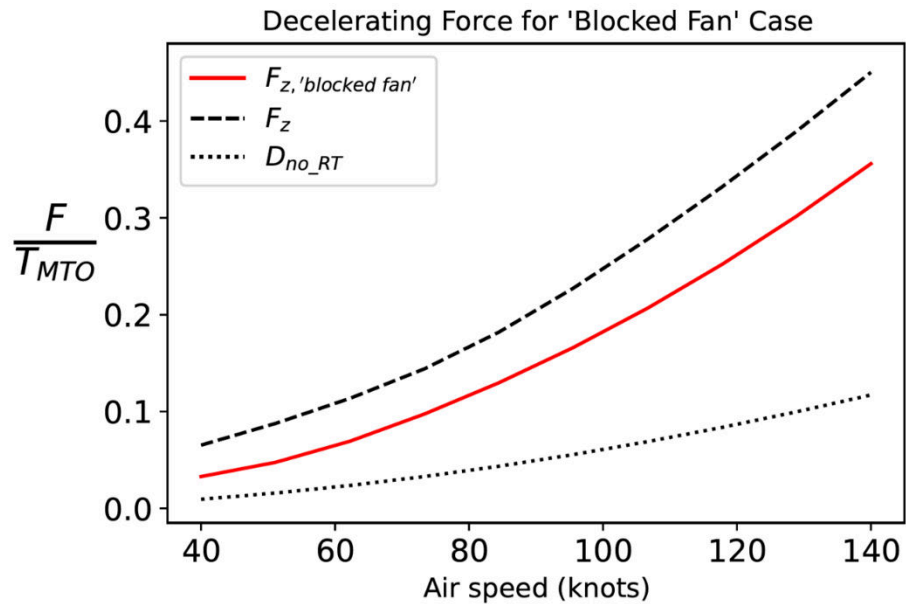


**FIGURE 8:** AXIAL DECELERATING FORCE FOR THE ‘BLOCKED FAN’ MODEL

The blockage effect is computed by subtracting the no reverse thrust baseline airframe drag from the decelerating force of the notional ‘blocked fan’ case ( $Blockage = F_{z,blocked fan} - D_{no\_RT}$ ). Then, the difference between the VPF contribution to reverse thrust,  $F_{RT}$ , and the blockage effect, is the flow reversal effect. However, the  $F_{RT}$  includes the penalizing effect of the constant core forward thrust due to the engine operation in the landing throttle setting throughout the aircraft landing run. This core thrust penalty is not included in the blocked fan case (through flow in the engine and core flow are not resolved in the ‘blocked fan’ model) and the no reverse thrust airframe drag calculation (the engine forward thrust bypass and core components are separated using standard bookkeeping control surface techniques to estimate the baseline airframe drag). Therefore, the flow reversal effect is corrected by adding

the core thrust ( $\sim 0.04T_{MTO}$  at landing setting) because the core forward thrust penalty is overcome by the flow reversal effect over and above the blockage effect to make up the VPF contribution to reverse thrust ( $Flow\ reversal = F_{RT} - Blockage + Core\ Thrust$ ).

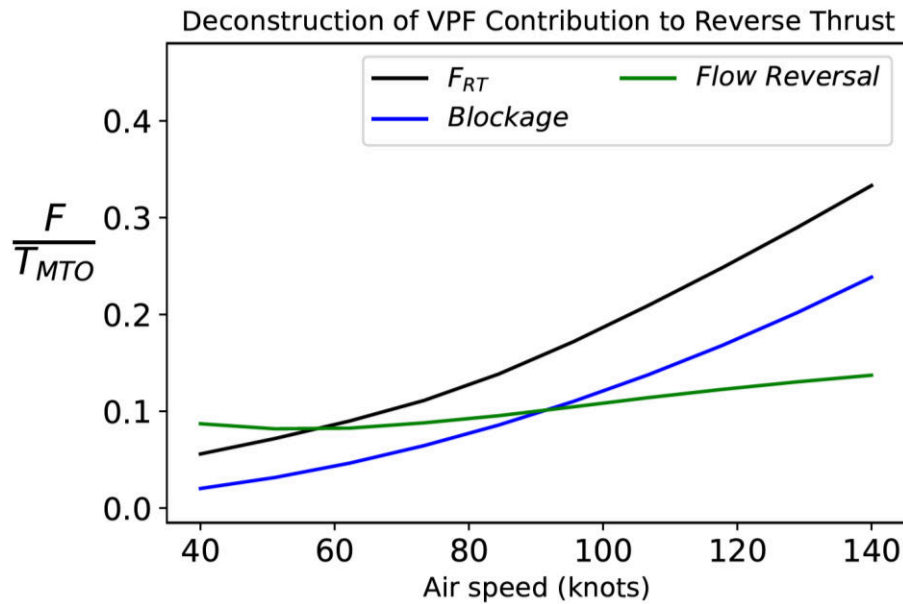


**FIGURE 9:** DECONSTRUCTION OF VPF CONTRIBUTION INTO BLOCKAGE AND FLOW REVERSAL EFFECTS

The blockage effect exhibits a dynamic pressure driven decreasing trend while the flow reversal effect remains nearly constant during the aircraft landing run. The flow reversal effect includes the increase in decelerating force due to momentum balance of reverse flow ingestion at bypass nozzle exit and ejection at fan inlet, the scrubbing shear interaction of high velocity, swirling reverse flow that is washed down towards the engine exit and the change in the blockage to the freestream flow spreading around the engine due to the washed down reverse flow shrouding the nacelle as shown in Figure 3. The reverse flow momentum balance exhibits only minor variations with the reduction in landing speed because the increase in reverse stream mass flow because of VPF suction acting on slower moving fluid in the engine exit regions is offset by the reduction in the velocity of the ingested reverse stream due to stream-tube stretching and the lower velocity of the capture stream from which the reverse flow develops. Additionally, the VPF reverse thrust flow field change with landing speed indicates a counteracting relation between the scrubbing shear interaction that dominates at higher landing speeds and the increase in blockage due to increased reverse flow shrouding that dominates at lower landing speeds. Consequent to the aforementioned flow field features dictated by the constant VPF operational setting during the landing run, the flow reversal effect remains nearly constant with the landing speed.

It is observed from the trends in the deconstructed components that: 1. The blockage effect dominates at higher landing speeds and represents up to two-thirds of the axial decelerating force at the aircraft touchdown speed of 140 knots. 2. The contribution of the

blockage effect decreases with the landing speed and the flow reversal effect dominates at lower speeds. Eventually at the limiting static conditions, the total  $F_z$  with the thrust reverser is due only to the flow reversal effect. Similar deconstruction trends are also observed for the different VPF settings in terms of stagger angle and rotational speed with differences observed only in the flow reversal effect while the blockage effect remains same.

### Lateral and Pitch Force Components

The VPF reverse thrust flow field results in secondary lateral force,  $F_y$ , and pitch force,  $F_x$ , components on the airframe during the aircraft landing run. The lateral and pitch force components for the VPF at  $\zeta_1^\circ$  stagger angle and  $N_1$  rotational speed setting during landing run is shown in Figure 10. The positive directions of the forces are shown in the inset of Figure 10. The  $F_x$  pitch force component is negative, which indicates a downforce that would aid the aircraft landing performance. The downforce component appears because of the upward deflection of streamlines that have escaped fan suction beyond the engine exit regions and its subsequent interaction with the wing as shown in the external flow field schematic of Figure 2. The downforce exhibits a typical dynamic pressure driven decreasing trend with the aircraft landing speed. The downforce magnitude varies from 11% to 4% of  $T_{MTO}$  in the thrust reverser engagement regime of 140 to 40 knots.

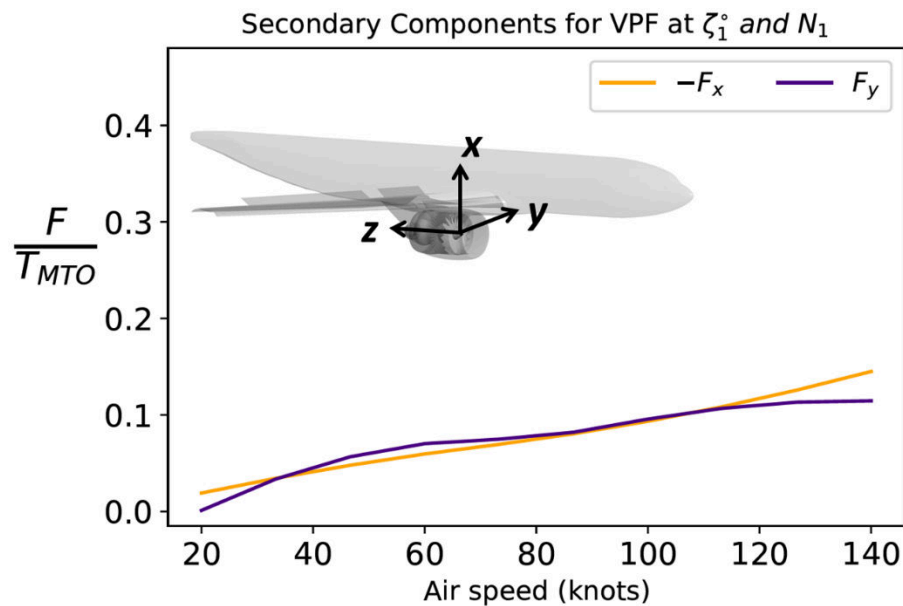


**FIGURE 10:** LATERAL AND PITCH FORCES FOR VPF AT  $\zeta_1^\circ$  STAGGER ANGLE AND  $N_1$  ROTATIONAL SPEED

The positive  $F_y$  lateral force component is a side force that points towards the airframe in the starboard engine and away from the airframe in the port engine in a co-rotating VPF arrangement. The lateral side force would be felt as a yawing moment on the airframe during the aircraft landing run. The swirling reverse flow streamlines from the fan inlet gets washed down at an angle by the freestream as it reaches the nacelle lip (shown in the external streamlines of Figure 3). As long as the streamlines remain attached over the nacelle

outer cover till a landing speed of 40 knots, the streamlines develop along at an angle till they encounter the pylon obstruction at the engine exit. In the starboard engine, the incidence of the washed down reverse stream flow on the pylon leaves a large separation on the wing inboard side towards the airframe. The extent of this separation zone is further bolstered by the swirling nature of the reverse flow development around the nacelle outer cover that causes a flow accumulation on the wing outboard side. In the port engine, when the direction of the fan rotation is like the starboard engine in typical circumstances, the angular sense of the washed down reverse flow streamlines incident on the pylon obstruction is same as the starboard engine. Consequently, the separation is formed in the wing outboard side away from the airframe. This flow non-uniformity behind the engine is responsible for the development of the lateral force.

The lateral force does not indicate a strong dynamic pressure dependence and remains at similar magnitudes as long as the washed down reverse flow streamlines remain attached to nacelle outer cover till a landing speed of 40 knots. Below the 40 knots speed, after the streamlines lift up from the nacelle lip to form the ‘peacock-dance’ flow field of Figure 3, the streamlines are no longer convected towards the engine exit at an angle. Consequently, the effect of pylon obstruction and resultant separation are not observed. This results in the magnitude of the lateral force to sharply decrease below 40 knots. The flow signature on a transverse plane that is downstream of the engine is shown in Figure 11 for 140 knots, where the streamlines remain attached and cause a lateral non-uniformity, and for 20 knots where the streamlines are lifted up and separation is not observed. The signature of flow acceleration in the engine lower nacelle surface due to the upward deflection of streamlines that have escaped fan suction and causes the downforce can also be noticed from Figure 11. The magnitude of the lateral force varies from 10% to 4% of  $T_{MTO}$  in the thrust reverser engagement regime of 140 to 40 knots.

Consequent to the presence of the secondary lateral and pitch force components during the VPF thrust reverser engagement, the resultant decelerating force vector on the airframe is deflected by a yaw angle,  $\cos^{-1}\left(\frac{F_y}{|F|}\right)$ , from the z-axis in the yz-plane, and a pitch angle,  $\cos^{-1}\left(\frac{F_x}{|F|}\right)$ , from the z axis in the xz-plane. The yaw and pitch angles of the resultant force vector for different aircraft landing speeds is shown in Figure 12 with insets indicating the change in the external flow field.

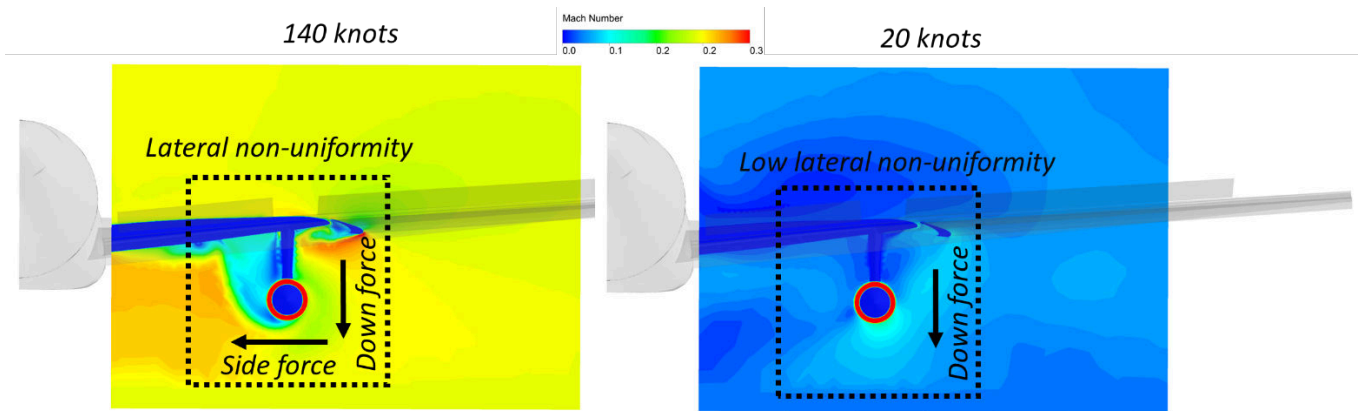


**FIGURE 11:** FLOW SIGNATURE RESPONSIBLE FOR SECONDARY FORCES AT ENGINE EXIT TRANSVERSE PLANE

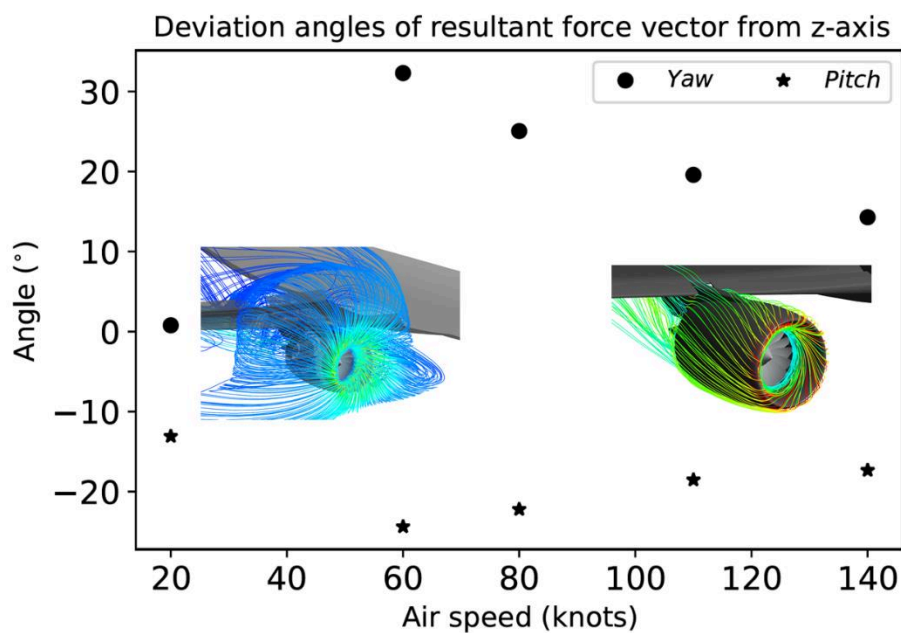


**FIGURE 12:** RESULTANT FORCE VECTOR DEVIATION FOR THE LANDING RUN

The yaw angle of the resultant force progressively increases with aircraft deceleration as long as the washed down reverse flow streamlines remain attached to the nacelle outer cover. This is because the magnitude of the lateral force remains relatively constant because of similar extents of flow non-uniformity at the engine exit plane while the axial decelerating force exhibits a dynamic pressure driven reduction. The pitch angle does not increase as significantly with landing speed. This is because both the downforce and the axial decelerating force exhibit similar dynamic pressure driven trends. However, the extent to which the dynamic pressure affects the upward bulk fluid deflection that is responsible for the downforce is smaller than the effect on the shear dominated axial decelerating force mechanisms. Therefore, a minor increase in the pitch angle with landing speed is observed. Both the yaw and the pitch angle exhibit a sudden discontinuous drop after the formation of the ‘peacock-dance’ flow field below 40 knots. The yaw angle becomes nearly  $0^\circ$  because of the significant reduction in the lateral non-uniformity at the engine exit plane. The pitch angle does not completely

disappear like the yaw angle. This is because the lateral outward spread of reverse flow streamlines near the ground in the ‘peacock-dance’ flow field only reduces and not blocks the washed down reverse flow that reaches the engine exit regions and are deflected. Therefore, the upward deflection of slower moving, lower amounts of flow near the engine exit causes a reduction in the pitch angle.

The change in the fan rotational speed from  $N_1$  to  $N_2=0.8N_1$  reduces the yaw angles by  $3^\circ - 4^\circ$  and the pitch angles by  $2^\circ - 3^\circ$  across the landing speed range. This is because the axial decelerating force,  $F_z$ , component is higher for the  $N_2$  rotational speed, as explained using Figure 5, while the lateral and downforce components remain similar because of similar generation mechanisms. The change in the VPF stagger angle setting from  $\zeta_1^\circ$  to  $\zeta_2^\circ = \zeta_1^\circ - 6^\circ$  increases the yaw angle by  $3^\circ - 4^\circ$ , while the pitch angle remains similar across the landing speed range. The increase in the yaw angle is driven by an increase in the swirl angle at which the flow exits the VPF inlet due to the change in the fan blade angle and the reverse flow within the fan passages. The increased swirl angle increases the angle at which the reverse flow streamlines are washed down at the nacelle lip and results in a larger lateral non-uniformity at the engine exit plane. The pitch angle is unaffected because the generation mechanism for the downforce is not significantly influenced by the change in the swirl angle due to the fan stagger angle.

### **Estimation of Uncertainties**

A qualitative numerical uncertainty estimation study is done to obtain a ‘reported uncertainty’ value for the parameters of interest based on the AIAA report for uncertainty management in computational aerodynamics [23]. The prediction metrics for the uncertainty study are the near field and far field force terms. The stack up of specific uncertainties due to domain discretization, convergence, and computation of parameters from the flow field vector solution space is used, rather than a typical differential perturbation analysis, to estimate the maximum error bands for parameters of interest and ensure the inherent uncertainty in the solution process is captured. The uncertainty bands from different sources are: 1. Domain discretization, which contributes up to 1% uncertainty, as obtained from the GCI study for local flow variables. 2. URANS convergence statistics and local flow periodicity driven temporal average estimates, which contribute up to 2% uncertainty. 3. Numerical integration and summation in the near field and far field methods, which contribute up to 2% uncertainty. The size resolution of the control surface in the far field methods, and the integral computations in high curvature, low projected area surfaces in the near field methods are the source of uncertainties in the numerical integration. A conservative sum-up of the individual uncertainty sources indicates that the maximum uncertainty in the estimated decelerating force and reverse thrust values is 5%. The conservative summative estimate of individual errors is chosen to account for second order numerical errors due to round-off and iteration in the solution algorithms. Additional uncertainties due to geometric modeling like the omission of landing gear and other minor external aircraft paraphernalia are excluded in the uncertainty estimates.

## Read Across to Other Designs

The use of VPF to generate thrust is a valuable proposition when it is used in future turbofan engines with high bypass ratios due to the potential cascade of benefits in weight reduction, performance and operability. In such high bypass ratio engines, the optimal fan design pressure ratios are below 1.3 from engine thermodynamic performance considerations. This study considers such a representative low-pressure ratio fan design that has been optimized for forward flow operation by considering typical modern flow coefficient and stage loading distributions. No additional reverse flow considerations are employed in the development of the fan design. The VPF reverse thrust behavior at a free stream velocity for this typical modern fan design correlates with the reverse stream flux development in and around the engine, which depends on the fan rotational speed and pressure ratio. Therefore, read across of the reverse flow results is applicable to similar low pressure ratio fans considered for high bypass ratio engines that are typical of current design practices. The 40000 lbf engine considered in the study has a diameter of  $\sim 110$  in and a bypass nozzle area of  $\sim 35$  ft<sup>2</sup>. The decelerating force and reverse thrust values are normalized with the maximum take-off thrust to enable comparison with other engine sizes. A typical 300-seater passenger commercial airframe with a wetted surface area of  $\sim 4400$  ft<sup>2</sup> is considered in this study. Standard scaling laws can be applied for equivalent airframe installations by computing effective increase in coefficient of drag of the baseline airframe. All the flow field computations are carried out at ISA, SL conditions and Mach numbers can be computed for non-dimensional read across to other cases.

## CONCLUSIONS

The resultant forces on the airframe with a VPF in reverse thrust mode during the aircraft landing run are estimated using a RANS/URANS flow field solution of a representative integrated airframe-engine-VPF model. The estimates of the resultant airframe forces in installed dynamic landing speed conditions as in this study, rather than the typical uninstalled, isolated static engine studies, are necessary to ascertain the feasibility of using VPF to generate reverse thrust. The outcomes from this study are:

1. The axial decelerating forces on the airframe for the complete thrust reverser engagement regime during the aircraft landing run are described for different VPF operational settings in terms of rotational speed and stagger angle. The computed axial decelerating forces are capable of achieving similar reduction in aircraft landing ground run distances as the conventional thrust reversers. The estimated values of the decelerating forces and its trends with the VPF operating parameters can aid in the choice of VPF reverse flow settings.



2. A notional ‘blocked fan’ analysis is described to separate and identify the extent of the key mechanisms, namely the blockage effect and the flow reversal effect, which contribute to the VPF reverse thrust. Such a break down provides a physical insight into the make-up of the decelerating forces and can be used for further design improvement studies.
3. In addition to the primary axial decelerating forces, secondary lateral and pitch force components due to the VPF reverse thrust flow field are identified and reported along with the description of the flow mechanisms responsible for their generation. The lateral force component points towards the airframe in the starboard engine and away from the airframe in port engine develops when both the engines are designed to have co-rotating VPF. This side force would appear as a yawing moment on the airframe during the landing run and would necessitate corrective rudder deflection during thrust reverser engagement. The pitch force component points downwards and would aid in the aircraft landing performance.
4. The estimate of the decelerating forces and the contributing flow mechanisms in the baseline airframe-engine-VPF configuration used in the study, which are typical of modern airframe-engine designs with no additional reverse thrust related design features provides a benchmark and handle for future VPF reverse thrust enhancement design modifications.

This work represents a step in the direction of successfully engineering a VPF to generate reverse thrust in future efficient, environment-friendly aircraft with high bypass ratio engines. Several design modifications that can provide control over the levels of decelerating force, manage the secondary force components, and avoid undesirable flow features have been investigated and are in the process of being filed as patents. Preliminary experimental arrangements for validating the flow field and force estimates are being considered for further exploration.

## **ACKNOWLEDGMENTS**

The authors would like to express their gratitude to Rolls-Royce plc. for supporting this research and for permission to publish the paper. Special thanks to Mr. John Whurr of Rolls-Royce plc. for comments and suggestions.

## **NOMENCLATURE**

### **Abbreviations**

ADP	Advanced Ducted Propulsor
GCI	Grid Convergence Index
ISA, SL	International Standard Atmosphere, Sea Level
OGV	Outlet Guide Vane

QCSEE	Quiet Clean Short-haul Experimental Engine
RHS	Right Hand Side
URANS	Unsteady Reynolds Averaged Navier-Stokes
VPF	Variable Pitch Fan

### **Symbols**

$N_1, N_2$	rotational speed
$D$	Drag
$E_D$	engine diameter
$F$	Force
$k$	turbulence kinetic energy
$n$	unit normal vector
$p$	pressure
$S$	elemental surface area
$T$	Thrust
$V$	velocity vector
$\zeta_1^\circ, \zeta_2^\circ$	stagger angle
$\rho$	density
$\tau$	shear stress tensor
$\phi$	far field integral term
$\omega$	specific dissipation rate

### **Subscripts**

$Far$	far field
$MTO$	Maximum Take-Off
$Near$	near field
$no\_RT$	no Reverse Thrust
$RT$	Reverse Thrust
$x$	pitch / up-down direction
$y$	lateral / transverse direction

$z$  longitudinal / drag direction

## REFERENCES

- [1] Mazzawy, R.S., 2010, October. Performance Study for the Benefits of a Variable Pitch Composite Fan. In Turbo Expo: Power for Land, Sea, and Air (Vol. 43963, pp. 37-45).
- [2] Krishnan, G., Perullo, C. and Mavris, D.N., 2013. An assessment of relative technology benefits of a variable pitch fan and variable area nozzle. In 49th AIAA/ASME/SAE/ASEE Joint Propulsion Conference (p. 3604).
- [3] Yang, X., Tang, H. and Chen, M., 2018. Performance modeling and optimization assessment of variable pitch fan for ultrafan engine. In 2018 Joint Propulsion Conference (p. 4400).
- [4] McKay, B. and Barlow, A., 2012, July. The ultrafan engine and aircraft based thrust reversing. In 48th AIAA/ASME/SAE/ASEE Joint Propulsion Conference & Exhibit (p. 3919).
- [5] Levin, K., Rich, D., Ross, K., Fransen, T. and Elliott, C., 2020. Designing and communicating net-zero targets. World Resources Institute. <https://www.wri.org/research/designing-and-communicating-net-zero-targets>
- [6] Topol, D.A., Ingram, C.L., Larkin, M.J., Roche, C.H. and Thulin, R.D., 2004. Advanced subsonic technology (AST) 22-inch low noise research fan rig preliminary design of ADP-type fan 3. NASA Glenn Research Center, Cleveland, OH, NASA Report No. CR-2004-212718. <http://ntrs.nasa.gov/search.jsp>.
- [7] Hobbs, D.E., Neubert, R.J., Malmborg, E.W., Philbrick, D.H. and Spear, D.A., 1995, Low Noise Research Fan Stage Design. NASA Scientific and Technical Information Branch, NASA-CR-195382
- [8] Williams, T.S. and Hall, C.A., 2019. Reverse Thrust Aerodynamics of Variable Pitch Fans. *Journal of Turbomachinery*, 141(8), p.081008.
- [9] Wright, G.H. and Russell, J.G., 1980. The M. 45SD-02 variable pitch geared fan engine demonstrator test and evaluation experience. *The Aeronautical Journal*, 84(836), pp.268-277.
- [10] Daly, M. and Gunston, B., 2010. *Jane's aero-engines-Issue 28*. IHS Jane's Verlag, ISSN, pp.1748-2534.
- [11] Rajendran, D.J., Bentley, D., Aguirre, H.A., Tunstall, R. and Pachidis, V., 2020. Development of a Research Model to Study the Operability of a Variable Pitch Fan Aero Engine in Reverse Thrust. *Global Power & Propulsion Society Chania 2020 Proceedings*, GPPS, Chania. <https://doi.org/10.33737/gpps20-tc-43>.
- [12] Rajendran, D.J. and Pachidis, V., 2019. Fan Flow Field in an Installed Variable Pitch Fan Operating in Reverse Thrust for a Range of Aircraft Landing Speeds. *Journal of Engineering for Gas Turbines and Power*, 141(10).

- [13] Rajendran, D.J. and Pachidis, V., 2021. Flow distortion into the core engine for an installed variable pitch fan in reverse thrust mode. *Journal of Turbomachinery*, 143(7), p.071001.
- [14] Rajendran, D.J. and Pachidis, V., 2021. On the Use of an Inflatable Rubber Lip to Improve the Reverse Thrust Flow Field in a Variable Pitch Fan. *Journal of Engineering for Gas Turbines and Power*, 143(11), p.111019.
- [15] Palmer, J.R., and Pachidis, V., 1990, The TURBOMATCH Scheme for Aero/Industrial Gas Turbine Engine Design Point/Off Design Performance Calculation, SME, Thermal Power Group, Cranfield University, UK.
- [16] Sarakinos, S.S., Lygidakis, G.N. and Nikolos, I.K., 2018. Flow Analysis of the DLR-F11 High-Lift Model Using the Galatea-I Code. *Journal of Aircraft*, 55(1), pp.355-372.
- [17] Blasco, D.C., 2017, 3D-CFD Model Design and Intergration of a Variable Pitch Fan Engine, M.Sc thesis, School of Aerospace, Transport & Manufacturing, Cranfield University.
- [18] Van Es, G.W., 2002. Rapid estimation of the zero-lift drag coefficient of transport aircraft. *Journal of aircraft*, 39(4), pp.597-599.
- [19] Nuic, A. and Mouillet, V., 2012. User manual for the base of aircraft data (BADA) family 4. European Organization for the Safety of Air Navigation (EUROCONTROL) TR, 12(11), pp.22-58.
- [20] PIANO User's Guide [online manual], Lissys LTd., Woodhouse Eaves, England, U.K., 2019, <http://www.piano.aero/>. [Accessed 15 August 2019].
- [21] McCullers, L.A., 1984. Aircraft configuration optimization including optimized flight profiles. NASA Scientific and Technical Information Branch, NASA N87-11743.
- [22] Scott C, A. and Jeffrey A, Y., 2000. Static Performance of Six Innovative Thrust Reverser Concepts for Subsonic Transport Applications-Summary of the NASA Langley Innovative Thrust Reverser Test Program. NASA Scientific and Technical Information Branch, NASA TM-2000-210300.
- [23] Luckring, J., Hensch, M. and Morrison, J., 2003, January. Uncertainty in computational aerodynamics. AIAA 2003-49, In 41st Aerospace Sciences Meeting and Exhibit (p. 409).

**APPENDIX – SCHEMATICS INDICATING VPF AEROFOILS TRANSITION TO REVERSE FLOW**

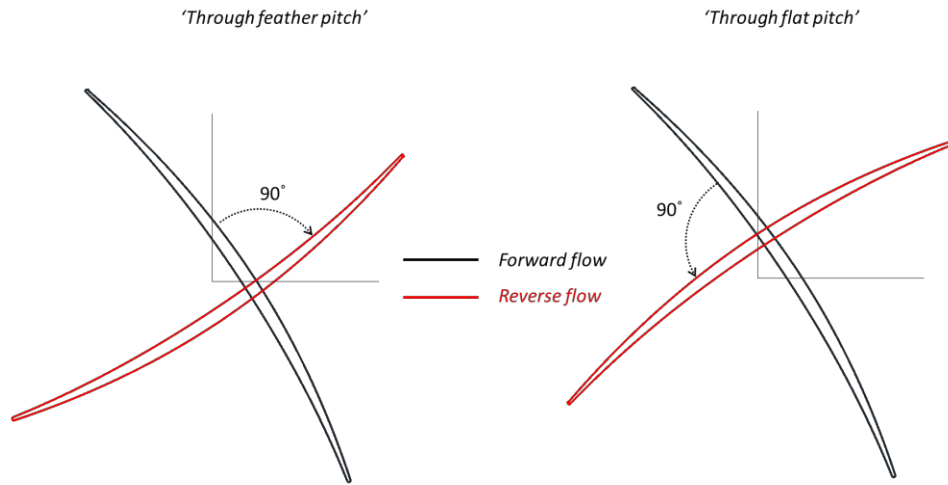


**FIGURE A1: 'THROUGH-FEATHER' AND 'THROUGH-FLAT' TRANSITION TO REVERSE FLOW MODE**

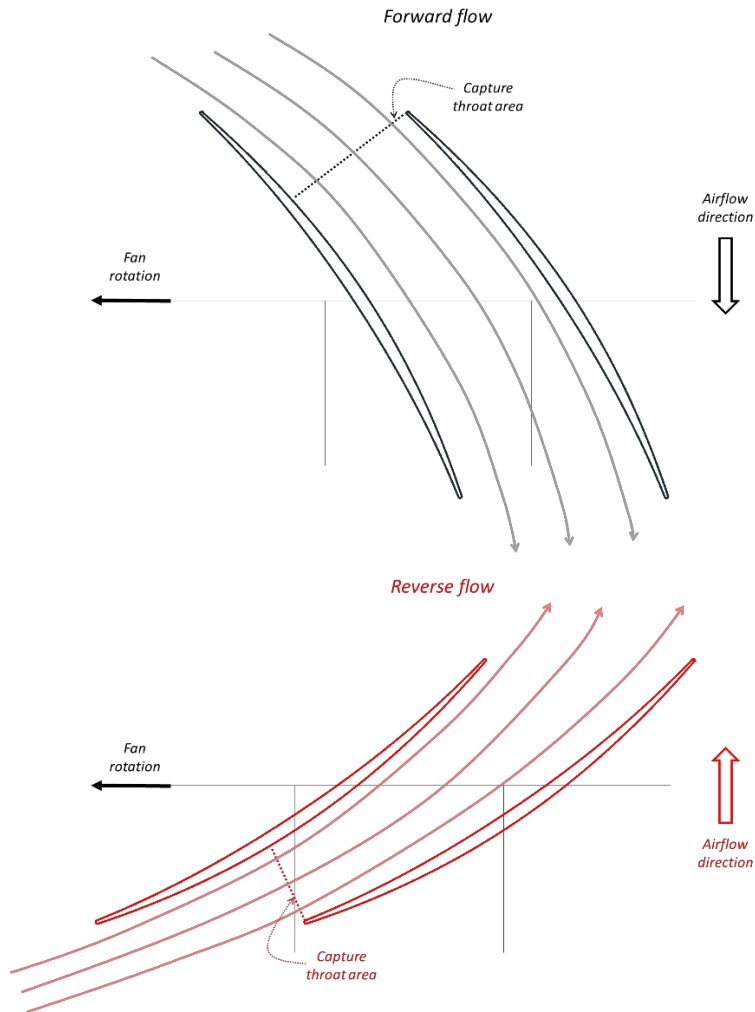


**FIGURE A2: VPF FORWARD FLOW AND REVERSE FLOW OPERATING MODES**

2022-10-28

# Estimation of resultant airframe forces for a variable pitch fan operating in reverse thrust mode

Rajendran, David John

American Society of Mechanical Engineers

---

Rajendran DJ, Tunstall R, Pachidis V. (2022) Estimation of resultant airframe forces for a variable pitch fan operating in reverse thrust mode. In: ASME Turbo Expo 2022: Turbomachinery Technical Conference and Exposition, 13-17 June 2022, Rotterdam, Netherlands. Paper number GT2022-82446

<https://doi.org/10.1115/GT2022-82446>

*Downloaded from Cranfield Library Services E-Repository*